



Cite this: *Nanoscale*, 2016, **8**, 458

## Highly stretchable MoS<sub>2</sub> kirigami

Paul Z. Hanakata,<sup>a</sup> Zenan Qi,<sup>b</sup> David K. Campbell\*<sup>a</sup> and Harold S. Park\*<sup>b</sup>

We report the results of classical molecular dynamics simulations focused on studying the mechanical properties of MoS<sub>2</sub> kirigami. Several different kirigami structures were studied based upon two simple non-dimensional parameters, which are related to the density of cuts, as well as the ratio of the overlapping cut length to the nanoribbon length. Our key findings are significant enhancements in tensile yield (by a factor of four) and fracture strains (by a factor of six) as compared to pristine MoS<sub>2</sub> nanoribbons. These results, in conjunction with recent results on graphene, suggest that the kirigami approach may be generally useful for enhancing the ductility of two-dimensional nanomaterials.

Received 18th September 2015,  
Accepted 20th November 2015

DOI: 10.1039/c5nr06431g

www.rsc.org/nanoscale

Molybdenum disulfide (MoS<sub>2</sub>) has been intensely studied in recent years as an alternative two-dimensional (2D) material to graphene. This interest has arisen in large part because (i) MoS<sub>2</sub> exhibits a direct band gap of nearly 2 eV in monolayer form which renders it suitable for photovoltaics,<sup>1</sup> and (ii) it has potential for many other technological applications, ranging from energy storage to valleytronics.<sup>2–5</sup>

The mechanical properties of MoS<sub>2</sub> have also been explored recently, through both experimental<sup>6–8</sup> and theoretical methods.<sup>9–12</sup> That MoS<sub>2</sub> has been reported experimentally to be more ductile than graphene<sup>8</sup> naturally raises the critical issue of developing new approaches to further enhancing the ductility of 2D materials.

One approach that has recently been proposed towards this end is “kirigami”, the Japanese technique of paper cutting, in which cutting is used to change the morphology of a structure. This approach has traditionally been applied to bulk materials and recently to micro-scale materials,<sup>13–15</sup> though recent experimental<sup>16</sup> and theoretical<sup>17</sup> works have shown the benefits of kirigami for the stretchability of graphene.

Our objective in the present work is to build upon previous successes in applying kirigami concepts to graphene<sup>17</sup> to investigate their effectiveness in enhancing the ductility of a different 2D material, MoS<sub>2</sub>, which is structurally more complex than monolayer graphene due to its three-layer structure involving multiple atom types. We accomplish this using classical molecular dynamics (MD) with a recently developed Stillinger-Weber potential.<sup>18</sup> We find that kirigami can substantially enhance the yield and fracture strains of monolayer

MoS<sub>2</sub>, with increases that exceed those previously seen in monolayer graphene.<sup>17</sup>

We performed MD simulations using the Sandia-developed open source code LAMMPS<sup>19,20</sup> and employing the Stillinger-Weber potential for MoS<sub>2</sub> of Jiang.<sup>18</sup> All simulations were performed on single-layer MoS<sub>2</sub> sheets. Of relevance to the results in this work, we note that while the Stillinger-Weber potential does not have a term explicitly devoted to rotations, it does contain two and three-body terms including angular dependencies, which are important for out-of-plane deformations. Furthermore, the Stillinger-Weber potential of Jiang<sup>18</sup> was fit to the phonon spectrum of single-layer MoS<sub>2</sub>, which includes both in and out-of-plane vibrational motions. As a result, the Stillinger-Weber potential should do a reasonable job of capturing out-of-plane deformations that involve angle changes, such as rotations.

The MoS<sub>2</sub> kirigami was made by cutting an MoS<sub>2</sub> nanoribbon, which had free edges without additional surface treatment or termination. A schematic view of the kirigami structure and the relevant geometric parameters is shown in Fig. 1. The key geometric parameters are the nanoribbon length  $L_0$ , the width  $b$ , the height of each interior cut  $w$ , the width of each interior cut  $c$ , and the distance between successive cuts  $d$ . We considered kirigami for both zig-zag (ZZ) and armchair (AC) edges. A representative AC MoS<sub>2</sub> kirigami consisting a number of  $N \sim 12\,000$  atoms with a nanoribbon length  $L_0 \sim 450$  Å, width  $b \sim 100$  Å, height of each interior cut  $w \sim 70$  Å, width of each interior cut  $c \sim 11$  Å, and distance between successive cuts  $d \sim 55$  Å is shown in Fig. 1.

The MD simulations were performed as follows. The kirigami was first relaxed for 200 ps within the *NVT* (constant number of atoms  $N$ , volume  $V$  and temperature  $T$ ) ensemble at low temperature (4.2 K), while non-periodic boundary conditions were used in all three directions. The kirigami was subsequently deformed in tension by applying uniform

<sup>a</sup>Department of Physics, Boston University, Boston, MA 02215, USA.

E-mail: dkcampbe@bu.edu; Tel: +1 617-353-1948

<sup>b</sup>Department of Mechanical Engineering, Boston University, Boston, MA 02215, USA.

E-mail: parkhs@bu.edu; Tel: +1 617-353-4208

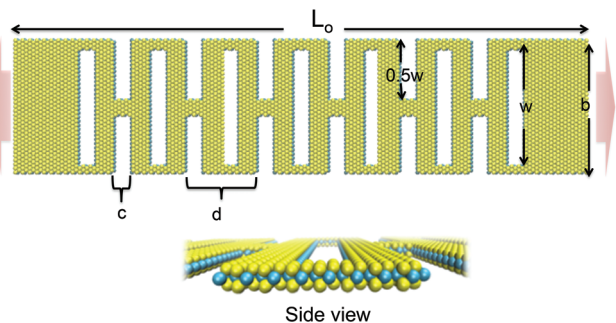


**Fig. 1** (Color online) Schematic of the MoS<sub>2</sub> kirigami, with key geometric parameters labeled. The kirigami is deformed via tensile displacement loading that is applied at the two ends in the direction indicated by the arrows. Top image represents a top view of the kirigami.

**Table 1** Comparison of mechanical properties of MoS<sub>2</sub> sheets and pristine nanoribbons in the armchair (AC) and zigzag (ZZ) direction

System	$\epsilon_f$	$\sigma_f^{3D}$ (GPa)	$Y^{3D}$ (GPa)
Sheet (AC)	0.178	16.8	154.0
Sheet (ZZ)	0.175	15.6	150.7
NR (AC)	0.130	14.6	145.8
NR (ZZ)	0.129	13.6	130.0

displacement loading on both ends, such that the kirigami was pulled apart until fracture occurred. We note that in actual applications, the MoS<sub>2</sub> kirigami will likely lie on a substrate, and thus adhesive interactions with the substrate may impact the deformation characteristics. In the present work, we focus on the intrinsic stretchability of the MoS<sub>2</sub> kirigami while leaving the interactions with a substrate for future work.

In addition, we simulated MoS<sub>2</sub> sheets (defined as monolayer MoS<sub>2</sub> with periodic boundary conditions in the plane) and pristine nanoribbons with no cuts for comparative purposes. The calculated fracture strains  $\epsilon_f$ , fracture stresses  $\sigma_f^{3D}$ , and Young's modulus  $Y^{3D}$  are tabulated in Table 1. The results are in reasonably good agreement with the experimental and first-principles studies of MoS<sub>2</sub> monolayer sheets.<sup>6,8 †</sup>

In Fig. 2(a), we plot a representative stress–strain curve of MoS<sub>2</sub> kirigami. For this, and the subsequent discussion, we introduce two non-dimensional geometric parameters  $\alpha = (w - 0.5b)/L_0$  and  $\beta = (0.5d - c)/L_0$ , which were also previously used to describe graphene kirigami.<sup>17</sup>  $\alpha$  represents the ratio of the overlapping cut length to the nanoribbon length, while  $\beta$  represents the ratio of overlapping width to the nanoribbon length. Put another way,  $\alpha$  describes the geometry orthogonal to the loading direction, while  $\beta$  describes the geometry parallel to the loading direction. Fig. 2(a) shows the stress–strain for the specific choices of  $\alpha = 0.0866$ , and  $\beta = 0.0375$ , which were

† In the above table, 3D stresses  $\sigma_f^{3D}$  are calculated as  $\sigma_f^{2D}/t_h$ , where  $t_h$  is the effective thickness with a value of  $\sim 6$  Å.

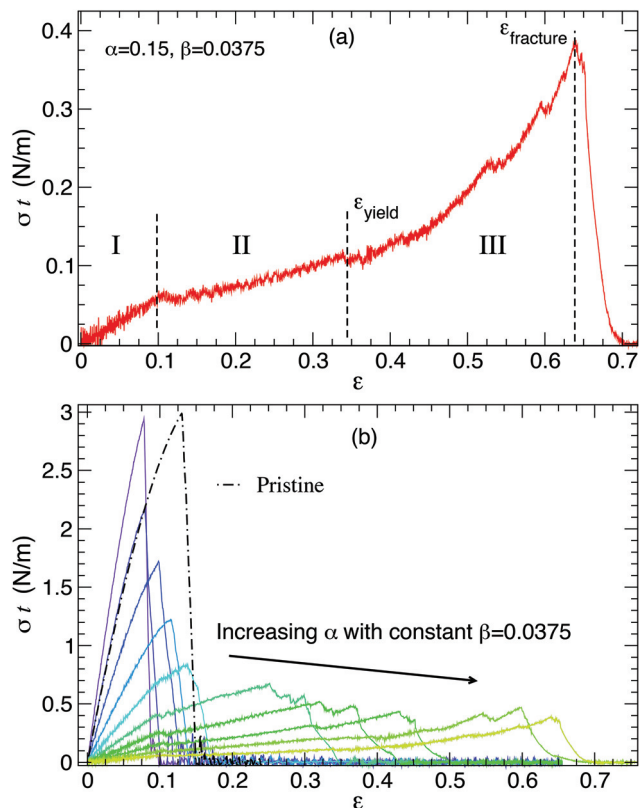


**Fig. 2** (Color online) Stress–strain curves of AC MoS<sub>2</sub> kirigami, where the 2D stress was calculated as the stress  $\sigma$  times the simulation box size  $t$ . (a) Stress–strain curve for constant  $\alpha = 0.0866$ ,  $\beta = 0.0375$ . (b) Stress–strain curve for AC kirigami keeping  $\beta = 0.0375$  constant and varying  $\alpha$ . Note the brittle fracture of the pristine MoS<sub>2</sub> nanoribbon. In general, the strain in region III increases substantially for  $\alpha > 0$ .

obtained by choosing  $b = 101.312$  Å,  $L_0 = 438.693$  Å,  $w = 88.648$  Å,  $c = 10.967$  Å, and  $d = 54.837$  Å. In contrast, Fig. 2(b) shows the change in the stress–strain response if  $\beta = 0.0375$  is kept constant while  $\alpha$  changes. This is achieved by changing  $w$  while keeping other geometric parameters constant. We also note that the 2D stress was calculated as stress (in direction parallel to the applied strain) times simulation box size perpendicular to the plane  $\sigma \times t$  to remove any issues in calculating the thickness,<sup>10</sup> while the stress was obtained using the virial theorem, as is done in LAMMPS.

It can be seen that there are generally three major stages of deformation for the kirigami, as separated by the dashed lines in Fig. 2(a). In the first stage (region I), the deformation occurs via elastic bond stretching, and neither flipping nor rotation of the monolayer MoS<sub>2</sub> sheet is observed, as shown in Fig. 3. In previous work on graphene kirigami, it was found that the kirigami rotates and flips in the first stage instead of stretching the bonds.<sup>17</sup> This does not occur for kirigami in MoS<sub>2</sub> in this first stage because the bending modulus of MoS<sub>2</sub> is nearly seven times higher than that of graphene.<sup>10</sup>

In the second stage (region II), for tensile strains ( $\epsilon$ ) exceeding about 10%, further strain hardening occurs. Kirigami patterning allows the MoS<sub>2</sub> monolayer to exhibit out-of-plane

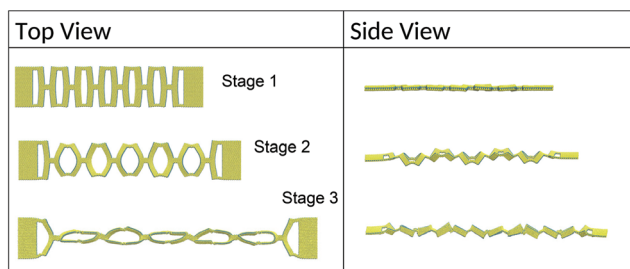


Fig. 3 Side and top views of kirigami during deformation.

deflections, as shown in Fig. 3, which permits the MoS<sub>2</sub> monolayer to undergo additional tensile deformation, which is in contrast to the brittle fracture observed for the pristine nanoribbon immediately following the initial yielding event, as shown in Fig. 2(b). Furthermore, the out-of-plane deflections cause the slope of the stress–strain curve in region II to be smaller than that in region I. This is because of the change in deformation mechanism from purely elastic stretching of bonds in region I, to a combination of stretching and out of plane buckling in region II.

Local bond breaking near the edges starts to occur at the tensile strain of  $\epsilon = 35\%$ . The occurrence of bond breaking is usually defined as the yield point, and signifies the demarcation between regions II and III. This local bond breaking occurs due to the concentrated stress at the edges connecting each slab, as previously observed in graphene kirigami.<sup>17</sup> At this stage, each kirigami unit is held by a small connecting ribbon which allows the monolayer to be almost foldable. Fig. 3 (stages 1 to 3) shows how the inner cut surface area having initial area  $w \times c$  and the height of the monolayer (largest out-of-plane distance between S atoms) can change significantly during the tensile elongation.

In the final stage, after more than 62.5% tensile strain, fracture and thus failure of the kirigami nanoribbon is observed. Unlike the pristine nanoribbon, the yield point can differ substantially from the fracture strain, and the difference increases with increasing cut-overlap, which was described previously, as shown in Fig. 2(b). Thus, it is important to quantify the yield point of the kirigami, as it defines the beginning of the irreversible deformation regime. Note that these regions vary depending on the kirigami structure, as shown in Fig. 2(b).

We also show, in Fig. 4, the von Mises stress distribution close to fracture at a tensile strain of 62%. In Fig. 4, the stress values were scaled between 0 and 1, and the stress distributions in the top S layer and single Mo layer were plotted separately for ease of viewing as MoS<sub>2</sub> has a tri-layer structure. We found that the largest stresses are concentrated near the edges of the each kirigami unit cell similar to our previous observation in graphene kirigami.<sup>17</sup>

Having established the general deformation characteristics for MoS<sub>2</sub> kirigami, we now discuss how the yield and failure characteristics depend on the specific kirigami geometry. We discuss the yield and fracture stresses and strains in terms of

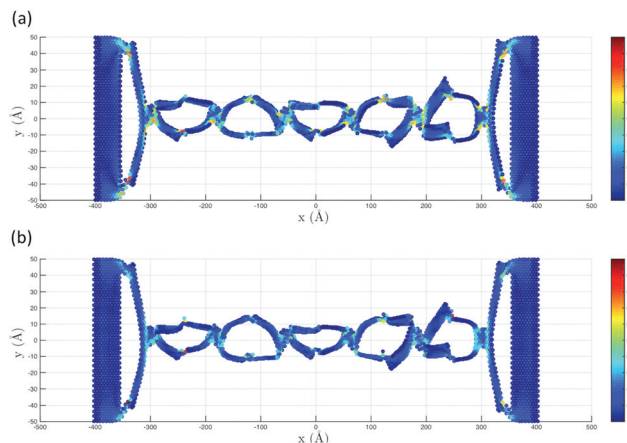


Fig. 4 Von Mises stress prior to the fracture at a tensile strain of 62% in (a) Mo layer and (b) top S layer of kirigami in Fig. 3. We plot the stress distribution layer by layer to give a clear picture of the stress distribution. The von Mises stress were scaled between 0 and 1.

the two geometric parameters  $\alpha$  and  $\beta$  that were previously defined.

The yield strain as a function of  $\alpha$  is shown in Fig. 5(a), while the yield stress as a function of  $\alpha$  is shown in Fig. 5(b). In these, and all subsequent figures, the stresses and strains are normalized by those for pristine MoS<sub>2</sub> nanoribbons of the same width so that the effect of the kirigami parameters can be directly quantified. As shown in Fig. 5, the MoS<sub>2</sub> kirigami becomes significantly more ductile for  $\alpha > 0$ , where the zigzag chirality reaches a yield strain that is about a factor of 6 larger than the pristine nanoribbon. In contrast, Fig. 5(b) shows that the yield stress for kirigami correspondingly decreases dramatically for increasing  $\alpha$ . We also note that the kirigami patterning appears to have a similar effect on the ductility of zigzag and armchair MoS<sub>2</sub> kirigami (shown in Fig. 5(a)), as the fracture strain and bending modulus of MoS<sub>2</sub> monolayer sheet in zigzag and armchair direction are similar.<sup>10,18</sup>

The increased ductility occurs because  $\alpha = 0$  corresponds to the case when the edge and interior cuts begin to overlap. Increasing  $\alpha$  above zero corresponds to when the edge and interior cuts do overlap, and thus it is clear that increasing the overlap increases the ductility of the MoS<sub>2</sub> kirigami. In contrast, the yield stress is higher for smaller  $\alpha$  because for negative  $\alpha$ , the edge and interior cuts do not overlap, and thus the deformation of the kirigami more closely resembles that of the cut-free nanoribbon.

In addition to the results of  $\alpha$ , the effect of  $\beta$  on the kirigami ductility is shown in Fig. 6(a) and (b). Specifically,  $\beta$  is varied by changing  $d$  while keeping other geometric parameters constant. For both the yield stress and strain,  $\beta$  does impact the yield stress and strain. Increasing  $\beta$  corresponds to an increase in the overlapping region width, which thus results in a smaller yield strain, and increased yield stress as compared to a pristine nanoribbon. For  $\beta \geq 0.03$ , we do not observe large differences between the AC and ZZ behavior in

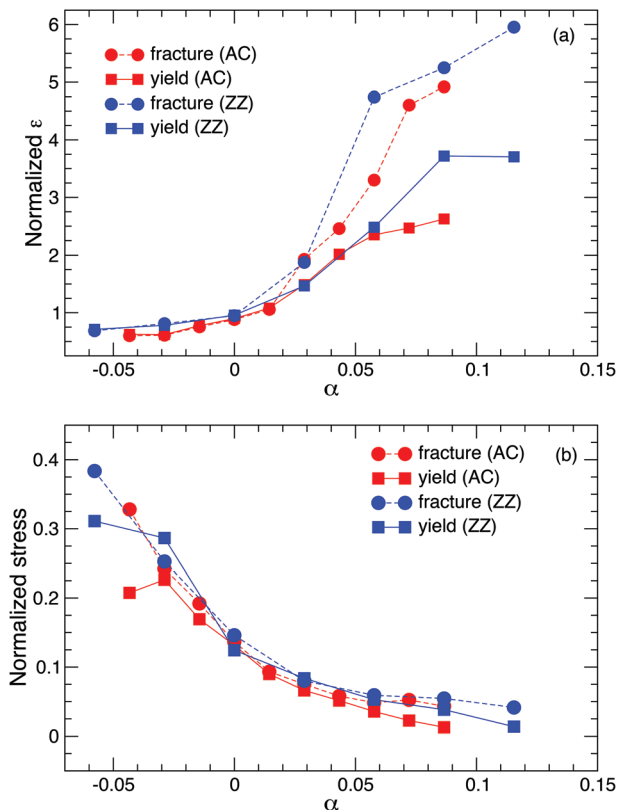


**Fig. 5** (Color online) (a) Influence of  $\alpha$  on yield and fracture strain for zigzag (ZZ) and armchair (AC) MoS<sub>2</sub> kirigami, with constant  $\beta = 0.0375$  for AC and constant  $\beta = 0.0417$  for ZZ. (b) Influence of  $\alpha$  on yield and fracture stress for zigzag (ZZ) and armchair (AC) MoS<sub>2</sub> kirigami. Data are normalized by MoS<sub>2</sub> nanoribbon results with the same width.

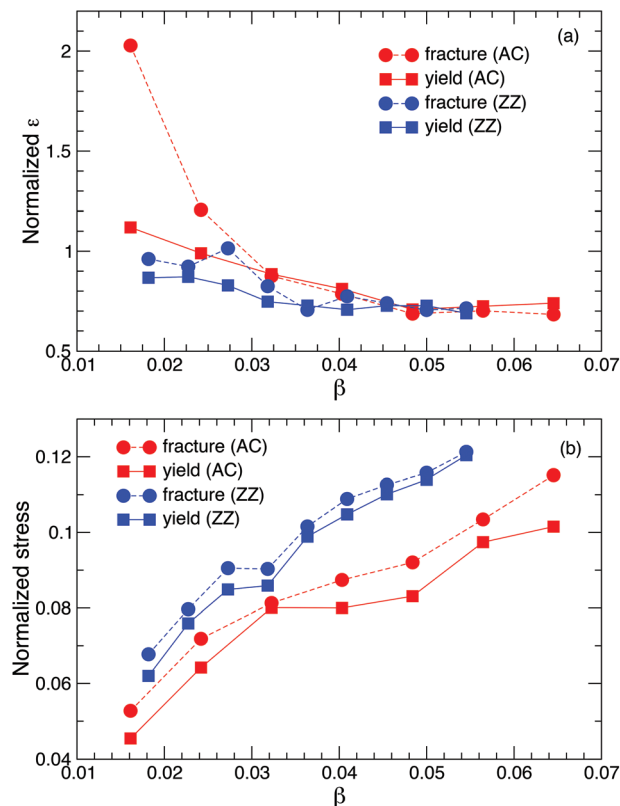


**Fig. 6** (Color online) Influence of  $\beta$  on the kirigami yield and fracture strain (a) and stress (b), with constant  $\alpha = 0.0186$  for AC and constant  $\alpha = 0.0157$  for ZZ. Data are normalized by MoS<sub>2</sub> nanoribbon results with the same width.

the case of varying  $\beta$  because increasing  $\beta$  (or decreasing the cut density) makes the kirigami more pristine, leading to similar values of fracture stress and strain in the AC or ZZ direction (see Table 1). Our results suggest that the failure strain can be maximized by increasing the overlapping cut (increasing  $\alpha$ ) and increasing density of the cuts (decreasing  $\beta$ ).

Recently, Guo *et al.* showed stretchability of metal electrodes can be enhanced by creating geometries similar to the ones illustrated in Fig. 1.<sup>15</sup> Adopting the geometric ratios determining fracture strain described in ref. 15, we found similar trends: the fracture strain increases with decreasing  $\frac{(b-w)}{c}$  and increases with increasing  $\frac{b}{d}$ . It is interesting to see that a similar trend is observed at a different length scale (an atomically-thin monolayer in this work as compared to  $a \approx 40$  nm thin film in the work of Guo *et al.*), and for a different material system (MoS<sub>2</sub> in this work, nanocrystalline gold in the work of Guo *et al.*), which suggests that the fracture strain in patterned membranes can be described entirely by geometric parameters.

It is also interesting to note that the yield and fracture strain enhancements shown in Fig. 5(a) exceed those pre-

viously reported for monolayer graphene kirigami.<sup>17</sup> The main reason for this is that the failure strain for the normalizing constant, that of a pristine nanoribbon of the same width, is smaller for MoS<sub>2</sub>. As shown in Table 1, this value is about 13%, whereas the value for a pristine graphene nanoribbon was found to be closer to 30%.<sup>17</sup> However, the largest failure strain for the MoS<sub>2</sub> and graphene kirigami were found to be around 65%, so the overall failure strains for graphene and MoS<sub>2</sub> kirigami appear to reach similar values.

In addition to the yield and fracture behavior, we also discuss the elastic properties, or Young's modulus. For the kirigami system, we expect the Young's modulus to decrease with increasing width of the cut  $w$  due to edge effects.<sup>9</sup> Fig. 7 shows the dependence of Young's modulus with effective width  $b_{\text{eff}} = b - w$ . As can be seen for both armchair and zigzag orientations, the modulus decreases nonlinearly with decreasing effective width, reaching a value that is nearly 200 times smaller than the corresponding bulk value for the smallest effective width value we examined. We introduce  $b_{\text{eff}}$  to have a more direct way of comparing the width of nanoribbons and kirigamis. This effective width  $b_{\text{eff}}$  is approximately proportional to the number of atoms in one unit cell of ribbons with cuts (kirigamis) or without cuts (pristine nanoribbons). Furthermore, the trend of the decrease differs from that pre-

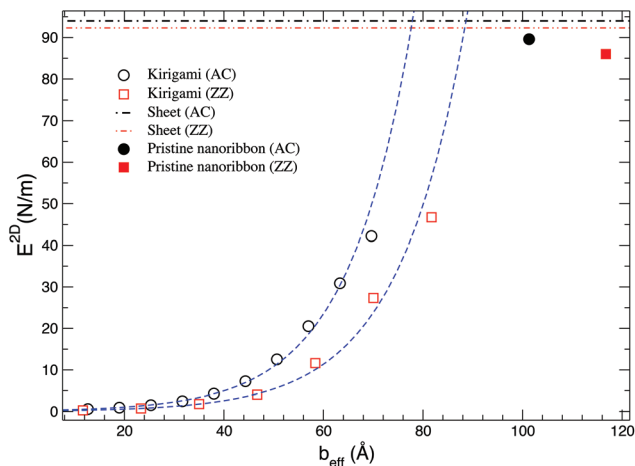


**Fig. 7** 2D Young's modulus  $E^{2D}$  of armchair (AC) and zigzag (ZZ) kirigami, pristine nanoribbons (PNR), and sheets. The fitting dashed line (colored blue) is given as a guide to the eye.

viously seen in graphene nanoribbons based on first principles calculations<sup>21</sup> and in MoS<sub>2</sub> nanoribbons based on atomistic simulations,<sup>9</sup> where a significantly more gradual decrease in stiffness was observed. This is due to the fact that for a given nanoribbon width  $b$ , the kirigami has significantly more edge area than a nanoribbon, leading to significant decreases in elastic stiffness even for effective widths  $b_{\text{eff}}$  that are close to the corresponding nanoribbon width.

Before concluding, we note that we have used the more recent Stillinger-Weber (SW15) potential of Jiang<sup>18</sup> rather than the earlier SW potential also developed by Jiang and co-workers<sup>9</sup> (SW13). This is because in comparing the tensile stress-strain curves, the SW15 potential more closely captured the trends observed in DFT calculations.<sup>8</sup> A comparison of the tensile stress-strain curve for monolayer MoS<sub>2</sub> is shown in Fig. 8 for the potentials of Jiang (SW15),<sup>18</sup> and Jiang *et al.* (SW13).<sup>9</sup> As shown by Xiong and Cao,<sup>22</sup> and also illustrated in Fig. 8, the earlier SW13 potential had a primary deficiency of exhibiting linear behavior at large strains, rather than the nonlinear elastic softening seen in DFT calculations. In contrast, the more recent SW15 potential, which we have used in the present work, exhibits the nonlinear elastic softening seen in DFT calculations.<sup>22</sup> Furthermore, the SW15 potential shows failure occurring around 20% tensile strain, in agreement with DFT calculations. These two facts show that the SW15 potential resolves the primary issue with the earlier SW13 potential, namely its accuracy at large strains close to failure.

We have also performed simulations of many kirigamis, nanoribbons, and monolayer sheets using the old SW potential. We have found qualitatively similar results with the very important difference that the SW13 potential predicts a tensile phase transition in pristine nanoribbon and monolayer sheet<sup>12</sup> that is not observed in the SW15 potential.<sup>18</sup>

In summary, we have applied classical molecular dynamics simulations to demonstrate that the kirigami patterning approach can be used to significantly enhance the tensile duct-

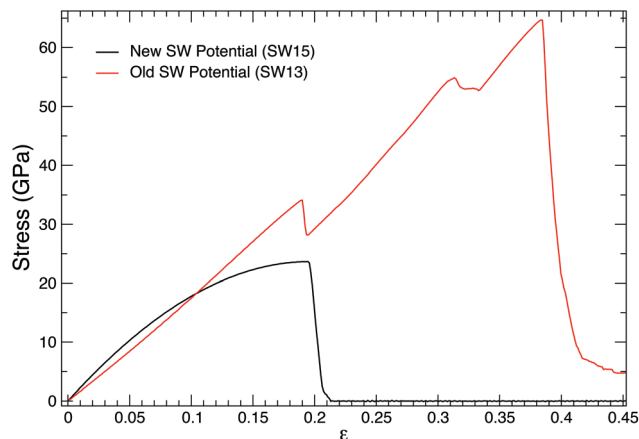


**Fig. 8** (Color online) Stress-strain curve of a monolayer MoS<sub>2</sub> sheet under tensile loading along the armchair direction using two different SW potentials. The newer SW potential<sup>18</sup> matches better with the trends observed in DFT calculations<sup>8</sup> than the first SW potential of Jiang *et al.*<sup>9</sup> No phase transition is observed with the more recent SW potential of Jiang<sup>18</sup>. For SW13, breaking of bonds between the Mo and S layers occur at  $\epsilon \sim 0.2$  and  $\epsilon \sim 0.3$  as observed in ref. 12.

ility of monolayer MoS<sub>2</sub>, despite the much higher bending modulus and rather more complex tri-layer structure of MoS<sub>2</sub> compared to graphene. The resulting enhancements in tensile ductility are found to exceed those previously reported for graphene.<sup>17</sup> These results suggest that kirigami may be a broadly applicable technique for increasing the tensile ductility of two-dimensional materials generally, and for opening up the possibility of stretchable electronics and photovoltaics using monolayer MoS<sub>2</sub>.

P. Z. H. and Z. Q. acknowledge the support of the Physics and Mechanical Engineering Departments at Boston University. D. K. C. is grateful for the hospitality of the Aspen Center for Physics which is supported by NSF Grant #PHY-1066293, and of the International Institute for Physics of the Federal University of Rio Grande do Norte, in Natal, Brazil, where some of this work was completed.

## References

- 1 K. F. Mak, C. Lee, J. Hone, J. Shan and T. F. Heinz, *Phys. Rev. Lett.*, 2010, **105**, 136805.
- 2 M. Chhowalla, H. S. Shin, G. Eda, L.-J. Li, K. P. Loh and H. Zhang, *Nat. Chem.*, 2013, **5**, 263–275.
- 3 Q. H. Wang, K. Kalantar-Zadeh, A. Kis, J. N. Coleman and M. S. Strano, *Nat. Nanotechnol.*, 2012, **7**, 699–712.
- 4 P. Johari and V. B. Shenoy, *ACS Nano*, 2012, **6**, 5449–5456.
- 5 H. Zeng, J. Dai, W. Yao, D. Xiao and X. Cui, *Nat. Nanotechnol.*, 2012, **7**, 490–493.
- 6 S. Bertolazzi, J. Brivio and A. Kis, *ACS Nano*, 2011, **5**, 9703–9709.
- 7 A. Castellanos-Gomez, M. Poot, G. A. Steele, H. S. J. van der Zant, N. Agrait and G. Rubio-Bollinger, *Adv. Mater.*, 2012, **24**, 772–775.

- 8 R. C. Cooper, C. Lee, C. A. Marianetti, X. Wei, J. Hone and J. W. Kysar, *Phys. Rev. B: Condens. Matter*, 2013, **87**, 035423.
- 9 J.-W. Jiang, H. S. Park and T. Rabczuk, *J. Appl. Phys.*, 2013, **114**, 064307.
- 10 J.-W. Jiang, Z. Qi, H. S. Park and T. Rabczuk, *Nanotechnology*, 2013, **24**, 435705.
- 11 K. Q. Dang, J. P. Simpson and D. E. Spearot, *Scr. Mater.*, 2014, **76**, 41–44.
- 12 J. Zhao, L. Kou, J.-W. Jiang and T. Rabczuk, *Nanotechnology*, 2014, **25**, 295701.
- 13 C. F. Guo, T. Sun, Q. Liu, Z. Suo and Z. Ren, *Nat. Commun.*, 2014, **5**, 3121.
- 14 T. C. Shyu, P. F. Damasceno, P. M. Dodd, A. Lamoureux, L. Xu, M. Shlian, M. Shtein, S. C. Glotzer and N. A. Kotov, *Nat. Mater.*, 2015, **14**, 785–789.
- 15 C. F. Guo, Q. Liu, G. Wang, Y. Wang, Z. Shi, Z. Suo, C.-W. Chu and Z. Ren, *Proc. Natl. Acad. Sci. U. S. A.*, 2015, **112**, 12332–12337.
- 16 M. K. Blees, A. W. Barnard, P. A. Rose, S. P. Roberts, K. L. McGill, P. Y. Huang, A. R. Ruyack, J. W. Kevek, B. Kobrin, D. A. Muller, *et al.*, *Nature*, 2015, **524**, 204–207.
- 17 Z. Qi, D. K. Campbell and H. S. Park, *Phys. Rev. B: Condens. Matter*, 2014, **90**, 245437.
- 18 J.-W. Jiang, *Nanotechnology*, 2015, **26**, 315706.
- 19 Lammmps, <http://lammmps.sandia.gov>, 2012.
- 20 S. Plimpton, *J. Comput. Phys.*, 1995, **117**, 1–19.
- 21 P. Wagner, C. P. Ewels, V. V. Ivanovskaya, P. R. Briddon, A. Pateau and B. Humbert, *Phys. Rev. B: Condens. Matter*, 2011, **84**, 134110.
- 22 S. Xiong and G. Cao, *Nanotechnology*, 2015, **26**, 185705.